

Chapter 13. Dynamics of nanoscale magnetic systems

13.1 Introduction to magnetization dynamics

The topic of nanoscale magnetic systems is broad and could easily provide enough material for an entire book on its own. In this chapter, as in previous ones, we will focus on the nanoscale magnetic systems for which near-field scanning microwave microscope (NSMM) measurement systems offer characterization capabilities that are difficult to achieve by other measurement techniques. Note then that the scope of such systems extends beyond ferromagnetic materials alone. For example, two-dimensional electron gases (2DEGs) in semiconductors, interfaces between complex oxide layers, and low-dimensional materials are also of interest. While building toward a discussion of NSMM measurements of magnetization dynamics, we will also review several complementary, broadband measurement techniques for characterization of micro- and nano-magnetic systems. At present, these complementary techniques are more mature than NSMM and more widely applied to magnetic systems. These include all-electrical measurements and magnetomechanical measurement techniques based on microelectromechanical systems (MEMS).

We begin with a brief summary of the theory of magnetization dynamics. We will limit our discussion to a phenomenological treatment in terms of classical mechanics. Historically, the development of reliable, microwave sources opened up the broad research field related to the motion of magnetization. It was discovered that for a given applied, static magnetic field the response of a magnetic material has a characteristic resonance behavior. Magnetic resonances may be measured by a variety of techniques, depending on the origin of the magnetic properties of the material. If the magnetic properties of a material arise from the electron and its spin, then the material may be investigated by electron paramagnetic resonance (EPR) and ferromagnetic resonance (FMR). If the source of the magnetic response is the nucleus, then the material may be investigated by nuclear magnetic resonance (NMR). Our focus will be on materials where the origin of the magnetic response is the electrons. Therefore, as we review the theory of magnetization dynamics, we will lay the groundwork for NSMM-based EPR and FMR applications.

Consider a single magnetic dipole placed in a static magnetic field. We will initially assume that this magnetic field is uniform. From the Lorentz force law, it follows that this magnetic moment will experience a torque that tends to align this moment with the direction of the applied magnetic field through damped precessional motion. Since the torque is the time derivative of angular momentum that is itself proportional to the magnetic moment, the equation of motion of the magnetization has the form

$$\frac{d\mathbf{M}}{dt} = -|\gamma|(\mathbf{M} \times \mathbf{H}_0) + \mathbf{R} \quad (13.1)$$

In the case of a single magnetic dipole, \mathbf{H}_0 is the applied, static external field, and \mathbf{M} is the magnetization (total magnetic moment) of the sample. The factor $|\gamma| = |-e|g/2m = g\mu_B/\hbar$ is called the gyromagnetic or magneto-mechanical ratio, g is the so called Landé spectroscopic splitting factor, e is the

electron charge, μ_B is Bohr magneton, and m is the mass of the particle. The value of $|\gamma|$ is $1.76 \times 10^{11} \text{ rad/s} \cdot T$ for an electron. For the nucleus, the value of γ depends on the mass and Landé factor of the nucleus. \mathbf{R} represents the damping in the system. Equation (13.1) is called the phenomenological equation of motion for magnetization or alternatively, the Landau-Lifschitz equation.

There are number of ways to introduce relaxation (losses) into this phenomenological formulation. The first one was originally proposed by Landau and Lifschitz in 1935 [1] in order to describe the motion of a domain wall in a ferromagnet. First, as they were considering the case of strongly coupled spin in a ferromagnetic material, they replaced the external field \mathbf{H}_0 with an effective field \mathbf{H}_{eff} that accounts for the sample shape, anisotropy and nearest neighbor interactions. Further, \mathbf{H}_{eff} represents the sum of static and the time-dependent, microwave magnetic field components. Thus, the effective field is expressed as a superposition of fields and relates to the total energy of the system E_{tot} as

$$\mathbf{H}_{eff} = -\frac{1}{\mu_0} \nabla_M E_{tot} = \mathbf{H}_0 + \mathbf{H}_{aniz} + \mathbf{H}_{dip} + \mathbf{H}_{ex} + \mathbf{H}_{me} + \mathbf{H}_{mel} + \mathbf{H}_{th} + \mathbf{h} \quad (13.2)$$

with $\mathbf{H}_0, \mathbf{H}_{aniz}, \mathbf{H}_{dip}, \mathbf{H}_{ex}, \mathbf{H}_{me}, \mathbf{H}_{mel}$, and \mathbf{H}_{th} corresponding to the external, anisotropy, dipolar, exchange, magneto-elastic, magneto-electric, and thermal fields, respectively. In addition, Landau and Lifshitz introduced a damping term that was derived based on thermodynamic considerations in the form

$$-\frac{\lambda}{M_s^2} (\mathbf{M} \times \mathbf{M} \times \mathbf{H}_{eff}) \quad (13.3)$$

This damping term implies that \mathbf{M} relaxes towards the static field direction at a rate, in a linear approximation, proportional to the dynamic precessional component $(\frac{d\mathbf{M}}{dt})_{Prec}$. Gilbert [2] proposed that the relaxation should occur at a rate proportional to total magnetization change of magnetization leading to a damping term in the form

$$\frac{\alpha}{M_s} (\mathbf{M} \times \frac{d\mathbf{M}}{dt}) \quad (13.4)$$

where α is a phenomenological constant, often referred to as the Gilbert damping parameter. In these formulations of the damping term, $\frac{d\mathbf{M}}{dt}$ is always normal to \mathbf{M} such that the absolute value of magnetization is conserved.

For EPR and NMR, where the coupling between the spins is not strong, the magnetization amplitude is not conserved and therefore it was necessary to independently introduce the spin-spin and spin-lattice relaxation times. This was done by Bloch in 1946 [3] and implemented for ferromagnetic resonance by Bloembergen in 1956 [4]. The Bloch equations have the form

$$\frac{dM_z}{dt} = -|\gamma| (\mathbf{M} \times \mathbf{H}_{eff})_z - \frac{M_z - M_s}{T_1} \quad (13.5a)$$

$$\frac{dM_{x,y}}{dt} = -|\gamma| (\mathbf{M} \times \mathbf{H}_{eff})_{x,y} - \frac{M_{x,y}}{T_2} \quad (13.5b)$$

In Equations (13.5), the static magnetic field is oriented in the z direction. T_1 is the spin-lattice or longitudinal relaxation time required for the z component of the magnetization M_z to relax into the field direction. T_2 is the spin-spin or transverse relaxation time for the transverse component of the magnetization $M_{x,y}$ that is related to the damping parameters introduced in Equations (13.3) and (13.4). Note that spin-spin relaxations cannot contribute to the relaxation of the z component.

In order to describe resonant phenomena, it is necessary to include the loss in the evaluation of the response. We will consider here harmonic time dependence in the small signal limit as these conditions are relevant for most NSMM measurements of magnetic materials (large signals and accompanying nonlinear effects are not discussed in this chapter). We will also assume that during the motion of the magnetization, all of the spins are in phase. This type of motion is called uniform precession and essentially can be modeled as a motion of a stiff vector that represents the total magnetization. Given these assumptions, the susceptibility tensor, which relates the dynamic component of the magnetization $\mathbf{M} = \mathbf{M}_0 + \mathbf{m}$ and the applied field \mathbf{h}_e , has the form

$$\mathbf{m} = [\chi_e] \cdot \mathbf{h}_e; [\chi_e] = \begin{pmatrix} \chi_e^x & -j\kappa_e \\ j\kappa_e & \chi_e^y \end{pmatrix}; \mathbf{b} = \mu_0(\mathbf{h}_e + \mathbf{m}) \quad , \quad (13.6)$$

where \mathbf{b} is the magnetic induction and μ_0 is the permeability of the vacuum. The external susceptibility tensor $[\chi_e]$ is related to the internal susceptibility tensor $[\chi]$ through the generalized demagnetizing factor $[\mathbf{N}]$, which accounts for sample shape and includes the influence of the anisotropy. The relation between external and internal susceptibilities is given by

$$[\chi_e] = ([I] - [\chi][\mathbf{N}])^{-1}[\chi] \quad , \quad (13.7)$$

where $[I]$ is the identity tensor. In the small signal limit, the components of the susceptibility tensor can be expressed in terms of the Gilbert damping parameter as

$$\chi_e^{x,y} = \frac{\omega_M(\omega_{x,y} + j\alpha\omega)}{\omega_x\omega_y - \omega^2 + j\alpha\omega(\omega_x + \omega_y)} = \chi_e'^{x,y} + j\chi_e''^{x,y} \quad , \quad (13.8a)$$

$$\kappa_e = \frac{-\omega_M\omega}{\omega_x\omega_y - \omega^2 + j\alpha\omega(\omega_x + \omega_y)} = \kappa_e' + j\kappa_e'' \quad , \quad (13.8b)$$

where

$$\omega_{x,y} = |\gamma|[H_0 + M_s(N_{x,y} - N_z)]; \omega_M = \gamma M_s; \omega_0 = |\gamma|H_0 \quad . \quad (13.9)$$

Further,

$$\omega_{FMR} = \sqrt{\omega_x\omega_y} = |\gamma|\sqrt{[\omega_0 + (N_x - N_z)\omega_M][\omega_0 + (N_y - N_z)\omega_M]} \quad (13.10)$$

is the well-known Kittel resonance condition [5]. The Gilbert damping parameter is related to the spin-spin relaxation time by

$$\alpha = \lambda/(|\gamma|M_s) = 2/[T_2(\omega_x + \omega_y)] \quad . \quad (13.11)$$

Note that the damping parameter in ferromagnets is not the same as the relaxation rate. From Equation (13.11) it follows that if the damping parameter is constant then the relaxation rate is shape dependent. Similar expressions can be obtained for the damping terms in other scenarios. In impulse-regime NMR and electron spin resonance (ESR), the Bloch equations have to be solved in the time domain and the usual approach involves transformation into a rotating reference frame. The generalization of the demagnetizing tensor $[\mathbf{M}]$ to include the anisotropy contribution can be found in Reference [6].

Uniform precession is a unique, special case among many possible magnetization excitations. If the motion of the magnetization is non-uniform throughout the sample, then it is necessary to consider additional solutions to the equation of motion for the magnetization. If the wavelength of the magnetization excitations is comparable to the sample dimensions, then electromagnetic boundary conditions have to be considered in addition to the equation of motion. As discussed in Chapter 2, Maxwell's equations are complemented by the materials equations. In such a case, the solution to Equation (13.8) enters the relation between the magnetic induction and the magnetic field through Equation (13.6). Most of the time, Maxwell's equations for this particular case are solved in the so-called "magnetostatic limit" that neglects the electric field contribution, but includes the electromagnetic boundary conditions. The resulting magnetostatic solutions take into account the sample shape and allow non-uniform motion of the magnetization throughout the sample volume. Furthermore, inclusion of the exchange interactions between the spins leads to the so-called magnetostatic-exchange solutions. The interested reader can further details in References [7] and [8].

Another case is presented when the wavelength of the magnetization excitations is much smaller than the sample dimensions. In this case, the electromagnetic boundary conditions at the surface of the sample can be neglected. Due to strong exchange coupling between the neighboring spins, the presence of defects or other material inhomogeneity, or non-uniformity of the external magnetic field will lead to a change of the relative phase in the motion of the neighboring spins. The solution of the equation of motion in this case takes the form of propagating modes. In the phenomenological approach, we express the dynamic variables -- the magnetization and the dynamic effective fields -- in terms of plane waves

$$\mathbf{m}(\mathbf{r}, t) = \sum_{\mathbf{k} \neq 0} \mathbf{m}_{\mathbf{k}}(t) e^{-j\mathbf{k} \cdot \mathbf{r}} \quad , \quad (13.12)$$

where \mathbf{k} is a wave vector of the particular excitation. The corresponding propagating waves of magnetization motion are called "spin waves." The introduction of the wave vector \mathbf{k} leads to more complicated relations for the frequencies of individual spin excitations that are functions of the wave vector. This gives rise to dispersion relations representing the functional dependence between the frequency (energy) and wave vector (momentum) that characterize non-uniform magnetization motion. Because these relations are inherently nonlinear, such an approach is useful for the investigation of dynamic, nonlinear magnetization effects. A full description of spin waves, their dispersion and interactions is beyond the scope of this work. A comprehensive study of magnetism and magnetization excitations can be found in the series edited by Rado and Suhl [9], and in References [10] and [11]. The equations introduced above provide a foundation for basic understanding of the nanoscale magnetic

processes and measurements discussed in this chapter. As needed, we will provide additional theoretical descriptions for specific cases.

13.2 Measurements of linear dynamics in microscale and nanoscale magnetic systems

13.2.1 Mechanical measurement of magnetization dynamics

The standard technique for investigation of magnetization dynamics is ferromagnetic resonance (FMR). In this measurement technique the material is biased with a static, external magnetic field and simultaneously exposed to a high-frequency electromagnetic field. As the electromagnetic radiation drives the magnetic precession at resonance, energy is absorbed by the system and dissipated via damping. This is manifest as changes in the transmission and reflection of incident radiation when the system is driven through resonance. From FMR measurements, one may subsequently determine the components of the magnetic susceptibility tensor. FMR may be carried out in a variety of experimental environments, including microwave cavities and on-wafer platforms. The microwave cavity approach has been described in numerous journal articles and books, including several referenced above. Reviews of on-wafer FMR measurement methods can be found in References [12] and [13], for example.

Here, we will focus on a slightly nonconventional technique for measurement of magnetization dynamics in small magnetic samples. Specifically, we are going to discuss measurement approaches in which a magnetic, thin film is integrated with a microcantilever. While, these approaches are not, strictly speaking, scanning probe methods, they illustrate the interaction of RF fields with magnetic probes. Contemporary magnetomechanical experiments are enabled by MEMS technology and are based on the fundamental physical fact that a change of angular momentum over time manifests itself as a torque. In the specific case of magnetic systems, changes in the magnetic moment are transduced to a mechanical torque. These approaches can be applied both to static and dynamic processes in small magnetic samples. Furthermore, these techniques take advantage of the facts that cantilevers are commercially available and that cantilever motion is detectable through interferometry and beam-bounce techniques. We will first introduce the principle of the experimental measurement and then we will show how it can be applied to measurement of magnetization dynamics.

The first measurement of gyromagnetic effects in macroscopic bodies was observed by Einstein and Haas [14]. They demonstrated that the mechanical rotation of an object could be induced by a change in the object's magnetization. The complementary effect -- induced magnetization by mechanical rotation -- was demonstrated soon afterward by Barnett [15]. The approach presented here extends the Einstein-de Haas experiment to microscale magnetic systems [16]. In the original experiment [14], the rotation of a macroscopic iron cylinder suspended by a glass wire was induced by applying an alternating magnetic field along the central axis of the cylinder. At the microscale, a thin magnetic film that is deposited on a micro cantilever takes the place of the iron cylinder [16]. In both cases, the alternating magnetic field induces a change in magnetic moment μ and a corresponding change in angular momentum J_{tot} . In order to satisfy the conservation of angular momentum, the changes in J_{tot} must be offset by changes in the mechanical angular momentum of the magnetic system. Thus, when an alternating magnetic field is applied perpendicular to the length of the cantilever, this change in angular momentum is manifest as a mechanical torque, leading to bending oscillations of the cantilever.

The absolute value of the magneto-mechanical ratio is defined as

$$g' = \frac{2m_e}{e} \frac{|\mu|}{|J_{tot}|} \quad (13.13)$$

where m_e is the electron rest mass. In Equation (13.13), J_{tot} includes contributions from both the spin and orbital angular momentum. The magneto-mechanical ratio is related to the gyromagnetic ratio g , which considers only spin angular momentum, through the following relation introduced by Kittel [17]

$$2 - g' = g - 2 \quad (13.14)$$

The magnetomechanical torque on the cantilever in the presence of the applied alternating field will bend the cantilever. The maximum magnitude of this torque is

$$T_0 = \frac{2m_e\omega}{eg'} \Delta\mu \quad (13.15)$$

where ω is the frequency of the alternating driving field and $\Delta\mu$ is the change of the magnetic moment. Experimentally, the deflection of the cantilever may be measured by use of optical interferometry, beam-bounce methods, capacitance measurements, or piezoresistive measurements, among other techniques. An example of the measured deflection as a function of the driving alternating field frequency is shown in Fig. 13.1. Note that the sensitivity of the technique is maximized when the alternating field frequency is close to the mechanical resonance frequency of the cantilever (about 13.2 kHz for the data shown in Fig. 13.1).

Figure 13.1. **Cantilever-based measurement of the Einstein de Haas effect.** Root mean square cantilever deflection measured by optical interferometry as a function of the applied alternating field frequency. The symbols represent the experiment and the solid line is the fit from Equation (13.16). The amplitude of the alternating magnetic field was 367 A/m and the resulting change in the magnetic moment of the film was estimated to be $\Delta\mu = 0.335$ nA m². Reprinted from T. M. Wallis, J. Moreland, and P. Kabos, *Appl. Phys. Lett.* **89** (2006) art. no. 122502, with permission from AIP Publishing.

By modeling the cantilever motion as a forced harmonic oscillator, it is possible to theoretically predict the deflection. In particular, a simple model of a force acting on a point mass at the free end of a rectangular cantilever beam leads to the following expression for the amplitude of the cantilever deflection:

$$z_0 = \frac{F_0/m_{mod}\omega}{\sqrt{(\omega_0^2 - \omega^2)^2/\omega^2 + \omega_0^2/Q^2}} \quad (13.16a)$$

where

$$F_0 = \frac{4m_e}{l_c eg'} \Delta\mu\omega \quad (13.16b)$$

m_{mod} is the modal mass of the cantilever beam, ω_0 is the resonance frequency of the beam, Q is the quality factor, and l_c is the length of the cantilever. Comparison of the predicted deflection with the experiment enables extraction of the magnetomechanical ratio. A more complete theoretical analysis of this problem was presented in Reference [18].

Having introduced the concept of measurement of magnetization dynamics by the Einstein-de Haas effect, we proceed to the measurement of magnetization dynamics by direct transfer of angular momentum from a microwave field to a mechanical system. This approach was introduced in References [19] and [20], in which the authors presented several approaches to mechanical measurements of magnetization dynamics. FMR was detected through three distinct effects. The first effect is the reduction of static magnetization when FMR conditions are met. The FMR is then detected as a change of magnetostatic torque acting on a sample in a magnetic field, as illustrated in Fig. 13.2(a). The second effect is the damping torque. This torque is the result of the damping process within a given material that produces a counter torque on the precessing spins, as illustrated in Fig. 13.2(b). Note that the first effect causing a bending motion of the cantilever while the second effect causes a torsional, twisting motion of the cantilever, provided that the orientations of the magnetization and external fields are as shown in Fig. 13.2. The final effect is heating of the sample due to the excitation of FMR, which results in the absorption of microwave energy by the spin system. When heated, the bimaterial system formed by the film and the cantilever will undergo a bending motion. The heating of bimaterial cantilever systems was also used in Reference [21] to map high-frequency, magnetic fields.

In order to understand how the first effect can lead to a mechanical torque, it is instructive to consider the case when the magnetic system is driven close to resonance. In the case of small damping ($\alpha \ll 1$) and near magnetic resonance, it is possible to assume that $\omega^2 \cong \omega_x \omega_y$. Under these conditions, the imaginary parts of the susceptibility tensor dominate. The relation between the magnetization components, m_x and m_y , and the external RF field in the x direction, h_x , can be expressed as

$$m_x = j\chi'' h_x \quad , \quad (13.17a)$$

$$m_y = \kappa'' h_x \quad . \quad (13.17b)$$

These two equations describe elliptical motion of the magnetization, schematically shown in Fig. 13.2(a). Note that the z direction is parallel to the long axis of the cantilever. Following Equations (13.8) and (13.9), the average steady state change of the magnetization in the z direction in the presence of an applied static field H_0 can then be expressed as

$$|\Delta M_z| \approx \frac{|m_x|^2 + |m_y|^2}{2M_s} = \frac{M_s h_x^2}{2\alpha(2H_0 + M_s)H_0} \quad . \quad (13.18)$$

Now, if an additional static magnetic torque field H_T is applied perpendicular to film plane, then this change in the z component of the magnetization results in a proportional change in the quasistatic magnetic torque

$$\Delta T_{stat} = \mu_0 \frac{H_T}{H_0} \frac{M_s}{2\alpha^2(2H_0 + M_s)} h_x^2 V \quad , \quad (13.19)$$

where V is the volume of the sample. This torque is directed in the x direction, causing a bending motion about the axis of the RF field. Note that this torque arises from the interaction of the DC component of the magnetic moment with the static torque field H_T .

Figure 13.2. **Magnetomechanical measurements of magnetization dynamics.** Illustration of two approaches to the mechanical measurement of the magnetization dynamics are shown: (a) the magnetostatic torque in a perpendicular field and (b) the damping torque. (c) Block diagram of instrumentation used for micromechanical, lock-in detection of magnetization dynamics in a magnetic system deposited on a cantilever. In this example, the RF field is provided by a stripline. Adapted from A. Jander, J. Moreland, and P. Kabos, *J. Appl. Phys.* **89** (2001) pp. 7086-7090, with permission from AIP Publishing.

The second effect that leads to a torque on the film-on-a-cantilever system comes from the direct interaction of the RF field component h_x with the dynamic, precessing component of the magnetization. Mathematically, this interaction takes the form of the cross product $\mathbf{m} \times \mathbf{h}$. If this product is evaluated with the respective components of \mathbf{m} and \mathbf{h} , then the average amplitude of the damping torque is obtained:

$$T_{damp} = \frac{1}{2} \mu_0 \kappa'' h_x^2 V = \frac{\mu_0 M_s}{2\alpha(2H_0 + M_s)} h_x^2 V \quad (13.20)$$

This is the torque that the microwave field must exert on the magnetization in order to maintain the precessional motion in the presence of damping. In the equilibrium state, this torque is transferred to cantilever and can be measured as a twist in the beam, as was shown in Reference [19].

The third and final effect that produces cantilever motion is the heating of the cantilever through FMR. The deposition of a magnetic, metal film on a Si cantilever forms a bimaterial system that will bend when heated due to the unequal thermal expansion of the two materials. The generated heat is proportional to the power absorbed by the magnetic system and can be expressed as

$$P = \frac{1}{2} \mu_0 \chi'' \omega h_x^2 V = \frac{\mu_0 M_s \gamma (H_0 + M_s)}{2\alpha(2H_0 + M_s)} h_x^2 V \quad (13.21)$$

A block diagram of the instrumentation used for micromechanical detection of FMR shown in Fig. 13.2 (c) and measurements are shown in Fig. 13.3. Fig. 13.3(a) shows the torsional motion from the damping torque measured as a function of the static bias magnetic field H_0 at a constant microwave field frequency of 9.15 GHz. The measurement clearly shows the characteristic torque response: the reversal in the sign of the torque signal as the orientation of the static bias field is switched. Fig. 13.3 (b) shows measurements of the bending motion from the power absorption at FMR for the same film. Note that there is no change in the sign of the response with changes in the sign of H_0 , as the thermal effect does not depend on the orientation of the static field. The thermal equilibration time of a typical, commercial Si cantilever is about 1 ms. Thus, thermally induced bending is challenging to detect at modulation frequencies above 1 kHz.

Therefore, to remove the thermal contribution to torque, measurements may be done at much higher modulation frequencies, usually corresponding to torsional resonant frequency of the cantilever that is on the order of ~ 250 kHz.

Figure 13.3. **Cantilever-based measurements of ferromagnetic resonance.** (a) FMR signal detected through measurements of cantilever torsion. (b) FMR signal detected by thermally-induced deflection that is proportional to the power absorbed by the magnetic system. Both measurements are shown as a function of the static magnetic field at the fixed microwave excitation frequency of 9.15 GHz. Reprinted from A. Jander, J. Moreland, and P. Kabos, *Appl. Phys. Lett.* **78** (2001) pp. 2348-2350, with permission from AIP Publishing.

Magnetomechanical measurement of dynamics have been extended to investigation of magnetization and spin dynamics in magnetic multilayers in Reference [22]. Specifically, the Einstein-de Haas effect was used to study interfacial spin transport, revealing the influence of the strong spin-orbit coupling in a Pt layer upon transfer of the angular momentum as a function of the applied static magnetic field. The measurements are shown in Fig. 13.4. The figure shows that the addition of a Cu layer to a permalloy (Py) film does little to change the cantilever deflection, but the addition of a Pt layer reduces the cantilever deflection roughly by a factor of two. This suggests a loss of the angular momentum through known spin-orbit interactions within the Pt layer and its subsequent absorption in the Pt layer. In classical FMR experiments, such interfacial interactions translate into an increase of the damping parameter. Here, the reduction in deflection amplitude is attributed to a clear transfer of angular momentum into Pt. This result demonstrates the sensitivity of the technique to the pure angular momentum transfer, or “spin flip” due to changes in interfacial transport at the boundary between the ferromagnetic and normal metal layers. The measured data agrees to first order with simple physical models that show that effective spin flip times are inversely proportional to the fourth power of the atomic number of the involved elements.

Figure 13.4. **Einstein-de Haas effect in multilayered structures.** Root mean square deflection of the cantilever as a function of the root mean square amplitude of a driving AC magnetic field in the presence of a 30 Oe (2.4 kA/m) static bias field for three structures: (1) Single-layer 50 nm Py, (2) Bi-layer 50 nm Py / 8 nm Cu, and (3) Bi-layer 50 nm Py / 8 nm Pt. Reprinted with permission, from S-H Lim, A. Imtiaz, T. M. Wallis, S. Russek, P. Kabos, Liufei Cai, and E M. Chudnovsky, *Europhys. Lett.* **105** (2014) art. no. 37009.

13.2.2 Time- and frequency-domain measurements of magnetization dynamics

Direct, broadband, electrical detection of magnetization dynamics at microscopic and nanoscopic length scales is challenging. The detection sensitivity is strongly dependent on the physical process used for detection. In this section, we will review several broadband and all-electrical methods for the

measurement of magnetization dynamics. Complementary methods such as time-resolved Kerr microscopy and x-ray techniques are also extensively used, but will not be addressed here. All-electrical measurement techniques include differential dV/dI resistance [23], [24], spin rectification effect [25], and RF/microwave transmission [26] techniques. These techniques are essentially modifications of broadband time- and frequency-domain measurements of submicron-sized magnetic systems. Often, the test platform takes the form of a coplanar or microstrip waveguide configuration. Time domain measurements of this type were introduced in Reference [27] and extended to the spectral domain in Reference [28]. In general, all-electrical techniques for characterization of single-layer magnetic systems are based on nonlinear coupling of microwave spin excitations with low-frequency charge currents through the anisotropic magnetoresistance effect.

A widely used approach is measurement of the differential resistance dV/dI of a micromagnetic system in response to a small AC current that alternates at a much smaller frequency than the magnetization precession frequency. The differential resistance is given by: $dV/dI = R + I dR/dI$. The first term R represents the DC resistance, while the second term represents reversible processes such as magnetization precession or magnetization switching. For anisotropic magnetoresistance, the resistance depends on the angle between the current direction and the sample magnetization direction. In general, the dependence is quite complicated and has a tensor form for single crystals. For polycrystalline samples, the anisotropic resistance can be expressed as a function of the angle θ between the current and field directions as

$$R_{MA}(\theta) = R_{\perp} + (R_{\parallel} - R_{\perp})\cos^2(\theta) \quad (13.22)$$

with R_{\parallel} and R_{\perp} corresponding to θ equal to zero degrees and ninety degrees, respectively. It is important to stress that any motion of the magnetization must be driven by microwave signals, but low-frequency modulation of the microwave signal is a practical strategy to enhance the signal-to-noise ratio by use of lock-in techniques.

Two additional all-electrical strategies for characterization of magnetization dynamics are measurements of the spin rectification effect and measurements of RF transmission. In the presence of a static magnetic field and a microwave fields oscillating close at a frequency ω near magnetic resonance, the angle θ is a function of time. Thus, the anisotropic resistance also varies in time. The measured voltage across the sample is then the product of the resistance and the current. This voltage will have the form of a constant term as well as terms with frequencies ω and 2ω . The constant term represents the spin rectification effect. The other terms represent the RF transmission, which can be measured by use of a high-frequency diode and a lock-in amplifier.

A comparison of dV/dI , RF transmission and spin rectification techniques on a simple microscale magnetic rectangular structure was presented in Reference [29]. All measurements were made with signal modulation and a lock-in technique. Fig. 13.5(a) shows the measured response of a rectangular, microscale element acquired with each of the three techniques during up-and-down field sweeps. The measured signals are characteristic of magnetic switching and show significant hysteresis. The abrupt change in dV/dI during the field sweep is attributed to vortex nucleation within the rectangular element. The RF transmission technique yields comparable results, with steps in the RF transmission occurring near

the same fields where steps occur in the dV/dI measurements. By contrast, the rectification technique has a similar signal-to-noise ratio to the other measurements, but the response is more complex and the interpretation is more complicated.

Figure. 13.5 **All-electrical measurements of patterned films.** (a) Measurements of a magnetic, $2\ \mu\text{m} \times 8\ \mu\text{m}$ rectangular element by use of (1) dV/dI , (2) RF transmission, and (3) spin rectification techniques. (b) FMR measurements of the same rectangular element by use of (1), (2) spin rectification measurements, (3), (4) RF transmission measurements, and (5) bridge circuit measurement. Vertical scales have been adjusted to facilitate comparison. Reprinted from S-H. Lim, T. M. Wallis, A. Imtiaz, D. Gu, P. Krivosik, and P. Kabos, *J. Appl. Phys.* **109** (2011) art. no. 07D317, with permission from AIP Publishing.

Fig. 13.5(b) compares FMR curves measured with each of these techniques. Curves (1), (2) were obtained by use of the rectification technique, curves (3), (4) by use of the transmission technique, and curve (5) by use of a RF transmission technique [29]. The FMR fields are marked by triangles and are found to be in good agreement with the predictions of Kittel's equation. From the comparison of the techniques, it follows that the transmission technique has poorer sensitivity and is the least effective technique for detection of FMR on lossy samples. This weakness is mitigated by implementing a bridge technique. To summarize, the three all-electrical detection techniques on micrometer-size ferromagnetic elements provide complementary information. The different approaches have different sensitivities for to specific magnetization dynamics, as shown by the contrasting sensitivities to vortex creation and FMR. Of the three techniques the spin rectification approach appears to be best suited for the broadband spectroscopy measurements, as it displays the best signal-to-noise ratio in both the low and high field ranges.

13.2.3 Measurements of magnetization dynamics in layered structures

The number of applications of magnetic multilayer structures exploded following the discovery of the giant magnetoresistance effect discovered by Albert Fert and Peter Gruenberg. In 2007, they were awarded the Nobel Prize for their discovery. The effect was observed in multilayered structures with alternating ferromagnetic and nonmagnetic layers. When such a multilayer structure is patterned to have nanometer dimensions and an AC or DC current is passed through it, the resulting response is due to both linear and nonlinear effects. These effects, including the giant magnetoresistive effect, provide a useful tool to measure the magnetic properties of these systems and the related magnetization dynamics. In particular, resistance measurements represent an effective, high-bandwidth method to measure magnetization dynamics. The resistance of two adjacent layers separated by nonmagnetic metal or thin dielectric spacer depends on the relative orientation of magnetizations in the neighboring layers. In most applications, the magnetization in one layer, the "fixed layer," is pinned in a fixed direction through exchange coupling while the magnetization in the other layer, the "free layer," is free to move with a

trajectory that depends on the coupling between the layers and any applied external fields. The resistance can be then expressed as [30]

$$R_{GMR}(\theta) = R_p + (\Delta R)(1 - \cos(\theta))/2 \quad (13.23)$$

where R_p is the resistance for parallel orientation and ΔR is the difference of the resistance between parallel and antiparallel magnetization orientation. The system of adjacent magnetic layers with one layer free to move with respect to a fixed layer is sometimes referred to as a “spin valve.”

Fig. 13.6 illustrates several approaches for the measurement of such structures. This versatile experimental configuration covers a broad range of possible measurement regimes, including DC, spectroscopic, frequency-domain and time-domain magnetization dynamics. The inductor and capacitor in the figure form a bias tee that allows separation of DC / low frequency signals from high frequency signals. Below, we specify which equipment and input excitations are utilized for the specific measurements.

Figure 13.6. Configuration for magnetoresistance measurements of spin valve structure. The spin valve is formed by a ferromagnet (F) / normal metal (N) / ferromagnet (F) structure. An RF signal line (RF) is placed in close proximity to the spin valve. The RF signal may be supplied by a pulse generator or vector network analyzer (VNA). The lower ferromagnetic layer is grounded while the other ferromagnetic layer may be used to supply a DC current (I_{DC}) or AC current (I_{RF}) to the spin valve. This upper layer also provides a detection path for RF signals by use of a VNA, high-speed oscilloscope, or spectrum analyzer. The orientation of static bias field (H_{bias}) and a pulse field (H_{pulse}) are also shown.

We begin with a consideration of the measurement of thermally excited FMR. For this particular measurement, among the components shown in Fig. 13.6, only the source of the DC current I_{DC} and the spectrum analyzer are required. This approach was used in References [31], [32] and [33]. When a DC current is sent through the spin valve, it will heat up slightly. The thermal fluctuations of the magnetization in the layers will lead to fluctuations of the resistivity that appear at the spectrum analyzer as noise. The noise power spectral density can be expressed as [29]

$$S_n(f) = (I_{DC}\Delta R)^2 \frac{2k_B T}{\pi f \mu_0 M_s^2 V} \chi''(f) = \frac{V_n^2}{R} \quad , \quad (13.24)$$

where $k_B = 1.38064 \times 10^{-23} m^2 kg s^{-2} K^{-1}$ is the Boltzmann constant, V is the volume of the element, ΔR is the resistivity change, and χ'' is the imaginary part of the susceptibility. From this dependence, it follows that the spectral noise density is proportional to the sample susceptibility, which has a resonant character. Therefore, the signal will show a resonance at the corresponding frequency of the natural FMR of the system. Fig. 13.7 shows the results of such measurement on a 20 gigabyte read head from a hard disk drive in the form of a noise spectrum. The resonance frequency near 4 GHz is clearly resolved.

Time-domain or spectral measurements may be performed by introducing an impulse generator or network analyzer as the source in the configuration shown in Fig. 13.6. The “detector” in Fig. 13.6 may be a diode detector, network analyzer, real-time oscilloscope or sampling oscilloscope. An example of time-domain, inductive measurements is shown in Fig. 13.7(b). The Fourier transform of the time-domain signal has a similar profile to the resonance curve shown in Fig. 13.7(a). From the Fourier transform, one can determine the resonance frequency as well as the losses in the system that are represented by the width at half magnitude of the resonance curve. Further, the resonance linewidth is directly related to damping parameters introduced in Equations (13.3) through (13.5). Fig. 13.7(c) shows the results of finite-element modeling of the magnetization response for a $0.8 \mu\text{m} \times 4.8 \mu\text{m}$ spin valve, which is in good agreement with the experimental data.

Figure 13.7. Time-domain measurements of magnetization dynamics in a hard disk head. (a) Spectral dependence of the voltage from a 20 Gb hard disk head. (b) Time domain impulse response. Reprinted from S. Kaka, J. P. Nibarger, S. Russek, N. A. Stutzke and S. L. Burkett, *J. Appl. Phys.* **93** (2003) pp.7539-7544, with permission from AIP Publishing. (c) The micromagnetic structure of the disk head is simulated by finite element simulations. The element is saturated when the impulse is applied (0 ns). Simulations are shown at two later times (0.12 ns and 0.31 ns) that correspond to peaks in the y component of the magnetization (M_y). The measurement (lower curve) is proportional to M_y .

In the thermally excited FMR measurements described above, a relatively small DC current passes through the layers. What happens when this current is increased? If the multilayer structure has lateral dimensions on the order of 100 nm or less, then new phenomena occur when the current exceeds a certain threshold level. As the current passes through the multilayer structure, the fixed layer serves as a spin filter, preferentially allowing electrons with spins parallel to the fixed-layer magnetization to flow through the structure. In the free layer, a spin torque will be exerted on spins that have a magnetization direction different from the fixed layer. This effect can lead to current-controlled hysteretic switching in magnetic nanostructures [34], [35], steady state magnetization precession, or excitation of ferromagnetic resonance. Spin-torque switching is currently being explored for use in ferromagnet-based random access memories. Spin-torque switching and precession was initially theoretically predicted Slonczewski and Berger [36], [37]. The measurement of the dynamic magnetization response of nanoscale multilayer magnetic systems due to spin torque may be carried out in a similar experimental configuration as the configuration described above for thermal FMR measurements. The experiment is done by applying a DC current to a structure and measuring the power spectral density with a spectrum analyzer or a diode detection system. The first experimental confirmation of DC current-induced magnetization precession due to this effect was presented in Reference [38]. This opened a broad research area into applications of nanoscale, nonvolatile oscillators. Detailed investigation of ferromagnetic resonance induced by DC currents are available in References [39] and [40].

Reference [41] introduced an alternative, particularly efficient method to measure the ferromagnetic resonance in magnetic nanostructures. Once again building on the configuration shown in Fig. 13.6, FMR in the nanostructure is driven by an AC current and the detection is done electrically by measurement of the DC voltage across the nanostructure. If both the DC current I_{DC} and RF current from a network analyzer are applied to a magnetic nanostructure at the same time, and the RF frequency is selected to be close to the ferromagnetic resonance frequency of one of the magnetic layers, then the magnetization in the layer will precess, resulting in time-dependent resistance $R(t)$. The resulting voltage $I(t)R(t)$ across the nanostructure will contain a DC component that can be expressed as

$$V_{DC} = I_{DC}(R_{DC} + \Delta R_0) + \frac{1}{2}I_{RF}\Delta R_f \cos(\theta_f) \quad . \quad (13.25)$$

θ_f is the phase of the mixing resistance. By modulating the microwave current I_{RF} and using a lock-in technique, the measurement isolates the second term, which depends upon the static magnetic bias field through the change in resistance ΔR_f , which is frequency dependent. In this way, one can measure the ferromagnetic resonance in these structures. Assuming a linear response of the system, the mixing voltage will have a simple Lorentzian line shape of the form [40]

$$V_{mix} = \frac{I_{RF}^2/\Delta_0}{1+[(f-f_0)/\Delta_0]^2} \quad , \quad (13.26)$$

where f_0 is the resonance frequency without the drive current and $\Delta_0 = \alpha f_0$ represents the damping of the system. A complete, detailed analysis of the line shape of the resonance curve obtained by this method is available in Reference [42].

In addition, electrical detection of magnetization dynamics includes the utilization of the concept of “spin pumping”, where the precession of the magnetization of a ferromagnet transfers spins into adjacent, normal-metal layers [43]. This “pumping” of spins produces a voltage in the normal metal that may be used as a measurement of spin wave dynamics in ferromagnetic metal/normal metal structures. Spin pumping has been used to explain observations of ferromagnetic resonance in ferromagnet/normal metal structures [44]. Furthermore, electrical characterization of the dynamics in nanomagnetic structures has led to the discovery of new effects such as the spin Hall [45] and inverse spin Hall effects [46]. These phenomena are also extensively used for characterization of ferromagnetic metals and ferrimagnetic dielectrics such as yttrium iron garnet (YIG) deposited on a normal metal. The experimental techniques that use these effects are essentially the same as described above with the difference that the voltage/resistance is measured at two electrodes connected to the normal metal layer. Ideally, the normal metal will have high spin-orbit coupling as is the case with Pt or Ta. The measured DC voltage is then the function of the magnetization dynamics at the interface between the nonmagnetic and ferromagnetic layers.

13.3 Scanning probe measurements of magnetization dynamics

In 1991, Sidles [47] proposed the measurement of proton spin through a nontraditional mechanical approach, which was later implemented by Rugar at IBM [48], [49] and culminated in application of this approach to single spin detection [50]. A schematic representation of this experiment is depicted in Fig.

13.8. A small permanent magnet is fixed on the end of a soft cantilever that is scanned over the specimen, an RF excitation field is provided by the coil, and the interaction of the cantilever with the sample is detected by an optical interferometer. The permanent magnet creates a local magnetic field that selects a constant-field slice in the sample within which the driving RF field can resonantly excite the spins. By changing the distance between the magnet and the sample or by changing the RF excitation field frequency, different slices of the sample are sampled and a three-dimensional tomograph may be reconstructed. The technique is known as magnetic resonance force microscopy (MRFM) and the approach triggered wide interest in the scanning probe community, including demonstrated applications to magnetic nanostructures [51], [52], semiconductors, and biological materials. MRFM is one of the few techniques that is capable of local electron paramagnetic resonance detection on nanometer or atomic scale. As of this writing, scanning probe methods that would be able to detect localized ESR signals remain a major challenge. Most of the standard, existing ESR methods are based on cavity or on-wafer methods.

Figure 13.8. **“Tip-on-cantilever” configuration for magnetic resonance force microscopy.** A small permanent magnet is fixed on the end of a soft cantilever that is scanned over the specimen, an RF excitation field is provided by the coil, and the interaction of the cantilever with the sample is detected by an optical interferometer. The hemisphere represents a slice within which the field is constant. Reprinted by permission from Macmillan Publishers Ltd: Nature. D. Rugar, R. Budakian, H. J. Mamin, and B. W. Chui, *Nature* **430** (2004) pp. 329-332. Copyright 2004.

Another early scanning probe approach for measurement of magnetization dynamics is based on the detection of microwave heating of the sample at resonance [53]-[55]. The technique may be considered as a specialized form of scanning thermal microscopy [56],[57]. At present, this approach, known as scanning thermal microscopy ferromagnetic resonance (STM-FMR), is a mature scanning probe technique that enables surface imaging as well as subsurface tomography [56]-[58]. The photoacoustic effect provides the mechanism for detection of the temperature increase in the sample. The photoacoustically detected microwave resonance provides no lateral resolution, but by changing the modulation frequency of the microwave input different subsurface depths can be distinguished. The complementary mirage effect provides a lateral resolution of about 50 μm for the measurement of the surface temperature. Further development of the technique was enabled by the incorporation of a temperature sensitive tip and by detecting local thermal expansion of the sample perpendicular to the surface. Together, these refinements have enabled imaging with 10 nm lateral spatial resolution. Fig 13.9 shows STM-FMR amplitude and phase images of Co stripes on Si taken at the resonance field of the backward volume mode [7], [8], which is defined as a mode that is propagating within the thin film with the direction of propagation along the static bias field. Here, this mode is propagating from the edge of the stripes. The scanned area shows a small cross section of the stripe.

Figure 13.9. **Scanning thermal microscopy – ferromagnetic resonance images.** STM-FMR Amplitude (left) and phase (right) images of Co stripes on Si obtained by use of STM-FMR at the resonance field of the backward volume mode. The imaging area is near the edge of the 100 μm x 2.5 μm x 0.01 μm Co stripe [58]. © IOP Publishing. Reproduced with permission. All rights reserved.

NSMM and related microwave and RF probing techniques provide yet another approach for local measurement of magnetic materials and magnetization dynamics. Though several early implementations of near-field scanning microwave probes were explicitly developed for characterization of magnetic materials [59], [60], the broader application of scanning microwave imaging to magnetic field detection has lagged behind the application to electric field detection. Early near-field probes were formed by opening a small aperture in a microwave waveguide. Following other aperture-based measurement approaches (described earlier in Chapter 8), the material of interest was brought close to the aperture and subsequently scanned back and forth to produce a near-field image. As techniques evolved, the apertures were replaced by specialized probe tips. For example, a magnetic field probe incorporates a specialized micro-machined cantilever that incorporates a conducting loop into an atomic force microscope system [61], [62], as shown in Fig. 13.10(a). The 6 μm -diameter loop acts as an inductive antenna that is sensitive to the perpendicular component of the magnetic field.

Figure 13.10 **Microwave probes for spatially-resolved measurements of magnetic systems.** (a) Schematic of microwave imaging system, including a scanning electron microscope image of the microfabricated probe. Reprinted from V. Agrawal, P. Neuzil, and D. W. van der Weide, *Appl. Phys. Lett.* **71** (1997) pp. 2343-2345, with permission from AIP Publishing. (b) Schematic of a coaxial ferromagnetic resonance micro-loop probe. The equivalent circuit for the probe-sample interaction is shown in the lower right. Reprinted from D. I. Mircea and T. W. Clinton, *Appl. Phys. Lett.* **90** (2007) art. no. 142504, with permission from AIP Publishing.

Fig. 13.10(b) shows an experimental configuration for the monitoring of high-frequency fields present above a microwave device by use of a network analyzer. This configuration can also be used for measurement of a dynamic magnetization response due to frequency- or time-domain excitation. This probe configuration enabled mapping of the permeability of the ferromagnetic material with about 100 μm lateral resolution. A similar configuration with a thin film Cu micro-loop deposited at the end of a coaxial cable has been applied in a similar way [63], [64]. At a given applied angular frequency $\omega = 2\pi f$, the probe-sample system can be modeled with a lumped-element model, also shown in Fig. 13.10(b). From this model, it follows that the total impedance at the terminal is

$$Z_T(f, H) \approx j\omega L_0(1 - k^2) + Z_S(f, H)k^2 \frac{L_0}{L_X} \quad , \quad (13.27)$$

where L_0 is the probe (loop) inductance, L_x is the inductance of the probe's image in the sample, Z_S is the complex surface impedance of the sample and k is a dimensionless coefficient describing the probe to-sample-coupling expressed through the mutual inductance M : $k = \sqrt{M^2/L_0L_x}$. The response of the magnetic sample is represented by the surface impedance that in the thin film limit can be expressed as

$$Z_S(f, H) = j\omega t_0 \mu_0 \mu_r(f, H) \quad (13.28)$$

where t_0 is the sample thickness and $\mu_r(f, H)$ is the complex permeability of the magnetic sample at a given frequency and static bias magnetic field. The total impedance is obtained from the measurement of the reflection coefficient $S_{11}(f, H)$ and comparing with the standard expression for the reflection coefficient (see Equation (3.3), for example). Note that the measurement can be done either at a constant bias field as a function of frequency or at a constant frequency as a function of the static bias magnetic field.

To reduce the influence of drifts that result from temperature changes in the electrical leads and the network analyzer, and to increase the signal-to-noise ratio, it is useful to obtain the permeability of the sample not from a single measurement, but rather from the difference between the measured total impedance at resonance and the measured total impedance off-resonance. The latter may be measured at a significantly higher or lower field value H_{OFFRES} than the resonance field H_{RES} . This procedure effectively subtracts the background response from the measurement. This difference can be done either with calibrated or non-calibrated scattering parameters obtained by use of the network analyzer. From (13.27), it then follows that

$$\Delta Z_T(f, H) = Z_T(f, H_{RES}) - Z_T(f, H_{OFFRES}) \quad (13.29)$$

The permeability then can be obtained from (13.27) and (13.29) as

$$\mu_r(f, H) \approx k^2 \frac{L_x}{L_0} \frac{1}{\omega t_0 \mu_0} [Im(\Delta Z_T(f, H)) - jRe(\Delta Z_T(f, H))] \quad (13.30)$$

This technique allows noncontact measurement of local magnetization dynamics and evaluation of a broad range of magnetic material properties. With only minor modifications, the loop-based, near-field probe can be applied to the local characterization of magnetization dynamics in many magnetic systems.

While scanning probe techniques described above are based on probes that utilize the loop as the sensing element, it is challenging to fabricate such probes in a way that is compatible with most contemporary NSMM systems, including homebuilt as well as commercial scanning probe instruments. Fig. 13.10(a) shows one method that is compatible with cantilever-based, commercial scanning probe systems. The design and fabrication of loop-based probes that fit common cantilever dimensions is challenging. Often, the loop geometry itself limits the lateral spatial resolution, which is typically tens of nanometers or less.

Therefore, there is strong interest in alternative sensing elements. It is well-known that the tunneling current of a scanned probe can be sensitive to magnetization state of the sample [65], [66]. Broadband measurement capability with scanning tunneling microscopy was introduced in Reference [67]. The techniques described therein enable the study of magnetization dynamics on the atomic scale. In

particular, it enables the measurement of electron spin relaxation times of individual atoms adsorbed on the surface using all-electronic, pump-probe techniques [68]. Measurements of single- and few-spin dynamics requires low temperatures and ultra-high-vacuum environments. Below, we will focus on experimental techniques that allow the measurement of the magnetization dynamics of nanoscale materials and devices under ambient temperatures.

A sharp STM or AFM tip can be modeled as an electric dipole. Therefore, in order to measure the magnetic response with a probe tip, the tip either has to be covered by a magnetic material as is the case in a magnetic force microscope (MFM) or the microwave dynamics have to be indirectly measured via the electric field resulting from the motion of magnetization. Unfortunately, readily available, MFM-compatible cantilevers are not suitable for measurements in the GHz frequency range. To circumvent this problem, the authors of Reference [69] positioned a 4 μm -diameter magnetic sphere onto a standard soft cantilever. This detector transduces the electromagnetic interaction of the sphere with the measured dynamic response of the sample into mechanical motion of the cantilever. Specifically, the force acting on the cantilever is proportional to the variation of the longitudinal magnetization component that varies due to excited dynamics in the sample such as ferromagnetic resonance.

The other option—measurement of the magnetization dynamics through the electric field component—is experimentally challenging, but it has been demonstrated that the dynamic magnetization response can be registered through the electric field generated by magnetization motion [70]. An open-ended, RF coaxial probe was used to detect the excitations of magnetostatic modes in a YIG disk by measurement of the reflection coefficient. A schematic diagram and an image of the probe are shown in Fig. 13.11(a) and 13.11(b), respectively. Fig. 13.11(c) shows frequency dependence of the reflection coefficient at several probe positions above the YIG sample at a constant magnetic field. For comparison, Fig. 13.11(c) also shows frequency dependence of the reflection coefficient for the same sample as obtained by use of a non-local, coplanar waveguide (CPW) measurement. The agreement of the probe-based measurements with the CPW-based measurements demonstrates the feasibility of measurement of the magnetization dynamics with electric field probe. The critical difference between the coplanar waveguide measurement and the probe measurement is that the scanning probe signal is obtained locally and the data can be used to reconstruct the spatial profile of the corresponding mode at a given resonance frequency, as shown in Fig. 13.11(d).

Figure 13.11. Coaxial probe measurements of an Yttrium Iron Garnet (YIG) disk. (a) Schematic and (b) photograph of the coaxial RF probe. (c) FMR signals detected from a YIG disk sample in the reflection spectra (S_{11}) with the RF probe positioned above the disk and a coplanar waveguide positioned under the disk. An in-plane, static magnetic field of 44 kA/m (550 Oe) was applied. The RF probe was located at three different positions above the YIG disk: $(x, y) = (0 \text{ mm}, 0 \text{ mm})$, $(3 \text{ mm}, 0 \text{ mm})$, and $(0 \text{ mm}, 3 \text{ mm})$; (d) reconstructed images of the corresponding modes. © 2010 IEEE. Reprinted, with permission from T. An, N. Ohnishi, T. Eguchi, Y. Hasegawa, and P. Kabos, *IEEE Magn. Lett.* **1** (2010) art. no. 3500104.

References

- [1] L. D. Landau and E. M. Lifschitz, "On the theory of dispersion of magnetic permeability in ferromagnetic bodies," *Physik Z. Sowietunion* **8** (1935) p. 153.
- [2] T. A. Gilbert, "Equation of motion of magnetization" *Armour Research Foundation Technical Report 11*, (1955).
- [3] F. Bloch, "Nuclear Induction," *Physical Review* **70** (1946) pp. 460-473.
- [4] N. Bloembergen, "Magnetic resonance in Ferrites," *Proc. I.R.E.* **44** (1956) p.1259.
- [5] C. Kittel, "On the theory of ferromagnetic resonance absorption," *Phys. Rev.* **73** (1948) pp. 155-161.
- [6] G. Srinivasan and A. Slavin, *High frequency processes in magnetic materials*, (World Scientific Publishing, 1995).
- [7] D. D. Stancil, *Theory of Magnetostatic Waves*, (Springer, 1993).
- [8] P. Kabos and V.S. Stalmachov, *Magnetostatic waves and their applications*, (Springer, 1994).
- [9] G. T. Rado and H. Suhl, *Magnetism*, (Academic Press, 1963).
- [10] B. Lax and K.J. Button, *Microwave ferrites and ferrimagnetism*, (McGraw Hill, 1962).
- [11] A.G. Gurevich and G.A. Melkov, *Magnetization Oscillations and Waves*, (CRC Press, 1996).
- [12] S. S. Kalarickal, P. Krivosik, M. Wu, C. E. Patton, M. L. Schneider, P. Kabos, T.J. Silva and J. P. Nibarger, "Ferromagnetic resonance linewidth in metallic thin films: Comparison of measurement methods," *Journal of Applied Physics* **99** (2006) art. no. 093909.
- [13] I. Neudeckera, G. Woltersdorf, B. Heinrich, T. Okuno, G. Gubbiotti, and C.H. Back, "Comparison of frequency, field, and time domain ferromagnetic resonance methods," *Journal of Magnetism and Magnetic Materials* **307** (2006) pp. 148–156.
- [14] A. Einstein and W. J. de Haas "Experimental proof of the existence of Ampère's molecular currents," *Koninklijke Akademie van Wetenschappen te Amsterdam, Proceedings*, **18** (1915) pp. 696–711 (in English) and *Verh. Dtsch. Phys. Ges.* **17** (1915) p. 152 (in German).
- [15] S. J. Barnett "Magnetization by rotation," *Physical Review* **6** (1915) pp. 239-270 (1915).
- [16] T. M. Wallis, J. Moreland, and P. Kabos, "Einstein-de Haas effect in NiFe film deposited on a microcantilever," *Applied Physics Letters* **89** (2006) art. no. 122502.
- [17] C. Kittel, "On the Gyromagnetic Ratio and Spectroscopic Splitting Factor of Ferromagnetic Substances," *Physical Review* **76** (1949) 743-748.
- [18] R. Jaafar, E. M. Chudnovsky, and D. A. Garanin, "Dynamics of the Einstein–de Haas effect: Application to a magnetic cantilever," *Physical Review B* **79** (2009) art. no. 104410.
- [19] A. Jander, J. Moreland, and P. Kabos, "Angular momentum and energy transferred through ferromagnetic resonance," *Applied Physics Letters* **78** (2001) pp. 2348-2350.
- [20] A. Jander, J. Moreland, and P. Kabos, "Micromechanical detectors for local field measurements based on ferromagnetic resonance," *Journal of Applied Physics* **89** (2001) pp. 7086-7090.
- [21] S. Lee, Y. C. Lee, T. M. Wallis, J. Moreland, and P. Kabos, "Near-field imaging of high frequency magnetic fields with calorimetric cantilever probes," *Journal of Applied Physics* **99** (2006) art. no. 08H306.
- [22] S-H Lim, A. Imtiaz, T. M. Wallis, S. Russek, P. Kabos, Liufei Cai, and E M. Chudnovsky, "Magneto-mechanical investigation of spin dynamics in magnetic Multilayers," *Europhysics Letters* **105** (2014) art. no. 37009.
- [23] S. Kasai, Y. Nakatani, K. Kobayashi, H. Kohno, and T. Ono "Current-driven resonant excitation of magnetic vortices" *Physical Review Letters* **97** (2006) art. no. 107204.
- [24] W. Lin, J. Cucchiara, C. Berthelot, T. Hauet, Y. Henry, J. A. Katine, E. E. Fullerton, S. Mangin, "Magnetic susceptibility measurements as a probe of spin transfer driven magnetization dynamics," *Applied Physics Letters* **96** (2010) art. no. 252503.

- [25] N. Mecking, Y. S. Gui, and C.-M. Hu, "Microwave photovoltage and photoresistance effects in ferromagnetic microstrips," *Physical Review B* **76** (2007) art. no. 224430.
- [26] Hanqiao Zhang, Axel Hoffmann, Ralu Divan, and Pingshan Wang, "Direct-current effects on magnetization reversal properties of submicron size Permalloy patterns for radio-frequency devices," *Applied Physics Letters* **95** (2009) art. no. 232503.
- [27] T. J. Silva, C. S. Lee, T. M. Crawford, and C. T. Rogers, "Inductive measurement of ultrafast magnetization dynamics in thin film Permalloy," *Journal of Applied Physics* **85** (1999) pp. 7849-7862.
- [28] A. B. Kos, T. J. Silva, and P. Kabos. "Pulsed inductive microwave magnetometer," *Review of Scientific Instruments* **73** (2002) pp. 3563-3569.
- [29] S-H. Lim, T. M. Wallis, A. Imtiaz, D. Gu, P. Krivosik, and P. Kabos, "Comparison of electrical techniques for magnetization dynamics measurements in micro/nanoscale structures," *Journal of Applied Physics* **109** (2011) art. no. 07D317.
- [30] E. Y. Tsymbal and D. G. Pettifor, "Perspectives of Giant Magnetoresistance," *Solid State Physics* **56** (2001) p. 113.
- [31] N. Smith and P. Arnett, "White-noise magnetization fluctuations in magnetoresistive heads," *Applied Physics Letters* **78** (2001) pp.1448-1450.
- [32] S. E. Russek and Sh. Kaka," Time and Frequency Domain Measurements of Ferromagnetic Resonance in Small Spin-Valve," *IEEE Transactions on Magnetics* **36** (2000), pp. 2560-2562.
- [33] S. Kaka, J. P. Nibarger, S. Russek, N. A. Stutzke and S. L. Burkett, "High-frequency measurements of spin-valve films and devices," *Journal of Applied Physics* **93** (2003) pp.7539-7544.
- [34] J. A. Katine, F. J. Albert, R. A. Buhrman, E. B. Myers, and D. C. Ralph "Current-driven magnetization reversal and spin-wave excitations in Co/Cu/Co pillars," *Physical Review Letters* **84** (2000) pp. 3149-3152.
- [35] E. B. Myers, D. C. Ralph, J. A. Katine, R. N. Louie, and R. A. Buhrman, "Current-induced switching of domains in magnetic multilayer devices," *Science* **285** (1999) pp. 867-870.
- [36] J. C. Slonczewski, "Current-driven excitation in magnetic multilayers," *Journal of Magnetism and Magnetic Materials* **159** (1996) pp. L1-L7.
- [37] L. Berger, "Emission of spin waves by a magnetic multilayer traversed by a current," *Physical Review B* **54** (1996) pp. 9353-9358.
- [38] M. Tsoi, "Excitation of a magnetic multilayer by an electric current," *Physical Review Letters* **80** (1998) pp. 4281-4284.
- [39] S. I. Kiselev, J. C. Sankey, I. N. Krivorotov, N. C. Emley, R. J. Schoelkopf, R. A. Buhrman and D. C. Ralph, "Microwave oscillations of a nanomagnet driven by a spin-polarized current" *Nature* **425** (2003) pp. 380-383.
- [40] W. H. Rippard, M. R. Pufall, S. Kaka, S. E. Russek, and T. J. Silva, "Direct-Current Induced Dynamics in Co₉₀Fe₁₀/Ni₈₀Fe₂₀ Point Contacts," *Physical Review Letters* **92** (2004) art. no. 027201.
- [41] J. C. Sankey, P. M. Braganca, A. G. F. Garcia, I. N. Krivorotov, R. A. Buhrman, and D. C. Ralph, "Spin-Transfer-Driven Ferromagnetic Resonance of Individual Nanomagnets," *Physical Review Letters* **96** (2006) art. no. 227601.
- [42] M. Harder, Z. X. Cao, Y. S. Gui, X. L. Fan, and C.-M. Hu," Analysis of the line shape of electrically detected ferromagnetic resonance," *Physical Review B* **84** (2011) art. no. 054423.
- [43] Y. Tserkovnyak, A. Brataas, and G. E. W. Bauer, "Enhanced Gilbert Damping in Thin Ferromagnetic Films," *Physical Review Letters* **88** (2002) art. no. 117601.
- [44] S. Mizukami, Y. Ando, and T. Miyazaki, "Effect of spin diffusion on Gilbert damping for a very thin permalloy layer in Cu/permalloy/Cu/Pt films," *Physical Review B* **66** (2002) art. no. 104413.
- [45] S. O. Valenzuela and M. Tinkham, "Direct electronic measurement of the spin Hall effect," *Nature* **442** (2006) pp. 176-179.
- [46] E. Saitoh, M. Ueda, H. Miyajima and G. Tatara, "Conversion of spin current into charge current at room temperature: Inverse spin-Hall effect," *Applied Physics Letters* **88** (2006) art. no. 182509.

- [47] J. A. Sidles, "Noninductive detection of single-proton magnetic resonance," *Applied Physics Letters* **58** (1991) pp. 2854-2856.
- [48] D. Rugar, C. S. Yannoni, J. A. Sidles, "Mechanical detection of magnetic resonance," *Nature* **360** (1992) pp. 563-566.
- [49] D. Rugar, O. Zuger, S. Hoen, C. S. Yannoni, H. M. Vieth, and R. D. Kendrick, "Force detection of nuclear magnetic resonance," *Science* **264** (1994) pp. 1560-1563.
- [50] D. Rugar, R. Budakian, H. J. Mamin, and B. W. Chui, "Single spin detection by magnetic resonance force microscopy," *Nature* **430** (2004) pp. 329-332.
- [51] Yu. Obukhov, D.V. Pelekhov, J. Kim, P. Banerjee, I. Martin, E. Nazaretski, R. Movshovich, S. An, T. J. Gramila, S. Batra, and P. C. Hammel, "Local Ferromagnetic Resonance Imaging with Magnetic Resonance Force Microscopy," *Physical Review Letters* **100** (2008) art. no. 197601.
- [52] M. M. Midzo, P. E. Wigen, D. Pelekhov, W. Chen, P. C. Hammel, and M. L. Roukes, "Imaging mechanisms of force detected FMR microscopy," *Journal of Applied Physics* **87** (2000) pp. 6493-6495.
- [53] R. Meckenstock, "Microwave spectroscopy based on scanning thermal microscopy: Resolution in the nanometer scale," *Review of Scientific Instruments* **79** (2008) art. no. 041101.
- [54] R. Meckenstock and J. Pelzl, "Investigation of anisotropy effects on interlayer exchange coupling by locally resolved photothermally modulated ferromagnetic resonance," *Journal of Applied Physics* **81** (1997) pp. 5259-5261.
- [55] R. Meckenstock, D. Spodding, D. Dietzel, J. Pelzl and J.P Bucher, "Scanning thermal microwave resonance microscopy of Ni nanodots," *Review of Scientific Instruments* **74** (2003) 789-791.
- [56] M. Nonnenmacher and H. K. Wickramasinghe, "Scanning probe microscopy of thermal conductivity and subsurface properties," *Applied Physics Letters* **61** (1992) pp. 168-170.
- [57] P. Tovee, M. Pumarol, D. Zeze, Kevin Kjoller, and O. Kolosov, "Nanoscale spatial resolution probes for scanning thermal microscopy of solid state materials," *Journal of Applied Physics* **112** (2012) art. no. 114317.
- [58] J. Pelzl and R. Meckenstock, "Photothermal investigation of local and depth dependent magnetic properties," *Journal of Physics: Conference Series* **214** (2010) art. no. 012002.
- [59] Z. Frait, V. Kambersky, Z. Malek, and M. Ondris, "Local variations of uniaxial anisotropy in thin films," *Czech. Journal of Physics B* **10** (1960) p. 616.
- [60] R. F. Soohoo, "A microwave magnetic microscope," *Journal of Applied Physics* **33** (1962) pp. 1276-1277.
- [61] V. Agrawal, P. Neuzil, and D. W. van der Weide, "A microfabricated tip for simultaneous acquisition of sample topography and high-frequency magnetic field," *Applied Physics Letters* **71** (1997) pp. 2343-2345.
- [62] B. T. Rosner and D. W. van der Weide, "High-frequency near-field microscopy," *Review of Scientific Instruments* **73** (1997) pp. 2505-2525.
- [63] R. Wang and M. Tabib-Azar, "Noncontact evanescent microwave magnetic dipole probe imaging of ferromagnets," *IEEE Transactions on Magnetics* **43** (2007) pp. 3165-3170.
- [64] D. I. Mircea and T. W. Clinton, "Near-field microwave probe for local ferromagnetic resonance characterization," *Applied Physics Letters* **90** (2007) art. no. 142504.
- [65] R. Wiesendanger, *Scanning Probe Microscopy and Spectroscopy: Methods and Applications*, (Cambridge University Press, 1994)
- [66] R. Schmidt, C. Lazo, H. Ho#lscher, U. H. Pi, V. Caciuc, A. Schwarz, R. Wiesendanger, and S. Heinze, "Probing the Magnetic Exchange Forces of Iron on the Atomic Scale," *Nano Letters* **9** (2009) pp. 200-204.
- [67] G. Nunes, Jr. and M. Freeman, "Picosecond Resolution in Scanning Tunneling Microscopy," *Science* **262** (1993) pp. 1029-1032.

- [68] S. Loth, M. Etzkorn, Ch. P. Lutz, D. M. Eigler, A. J. Heinrich, "Measurement of Fast Electron Spin Relaxation Times with Atomic Resolution," *Science* **329** (2010) pp. 1628-1630.
- [69] G. de Loubens, V. V. Naletov, M. Viret, and O. Klein, H. Hurdequint, J. Ben Youssef, F. Boust, N. Vukadinovic, "Magnetic resonance spectroscopy of perpendicularly magnetized Permalloy multilayer disks," *Journal of Applied Physics* **101** (2007) art. no. 09F514.
- [70] T. An, N. Ohnishi, T. Eguchi, Y. Hasegawa, and P. Kabos, "Local Excitation of Ferromagnetic Resonance and Its Spatially Resolved Detection with an Open-Ended Radio-Frequency Probe," *IEEE Magnetics Letters* **1** (2010) art. no. 3500104.

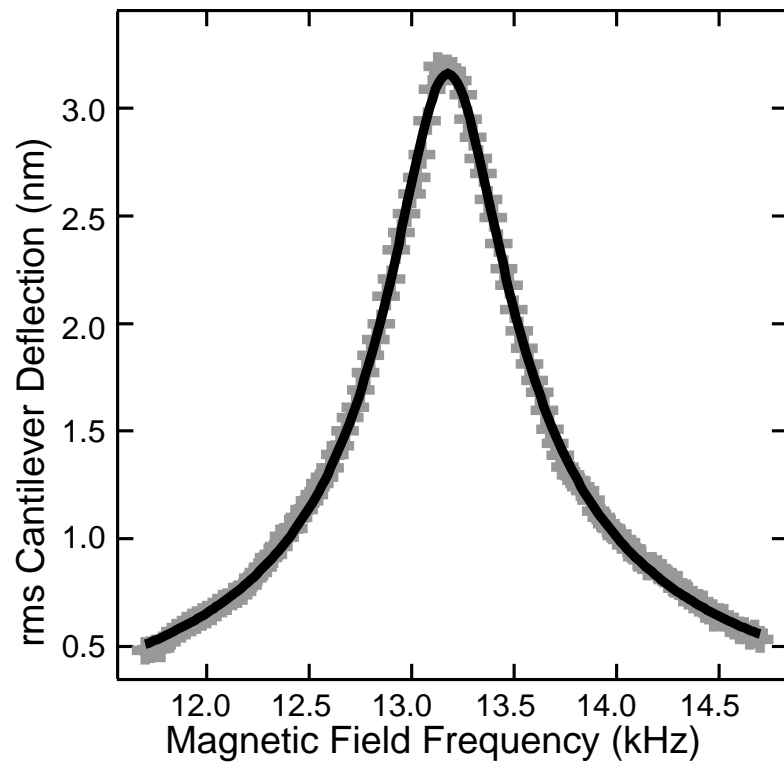


Figure 13.1

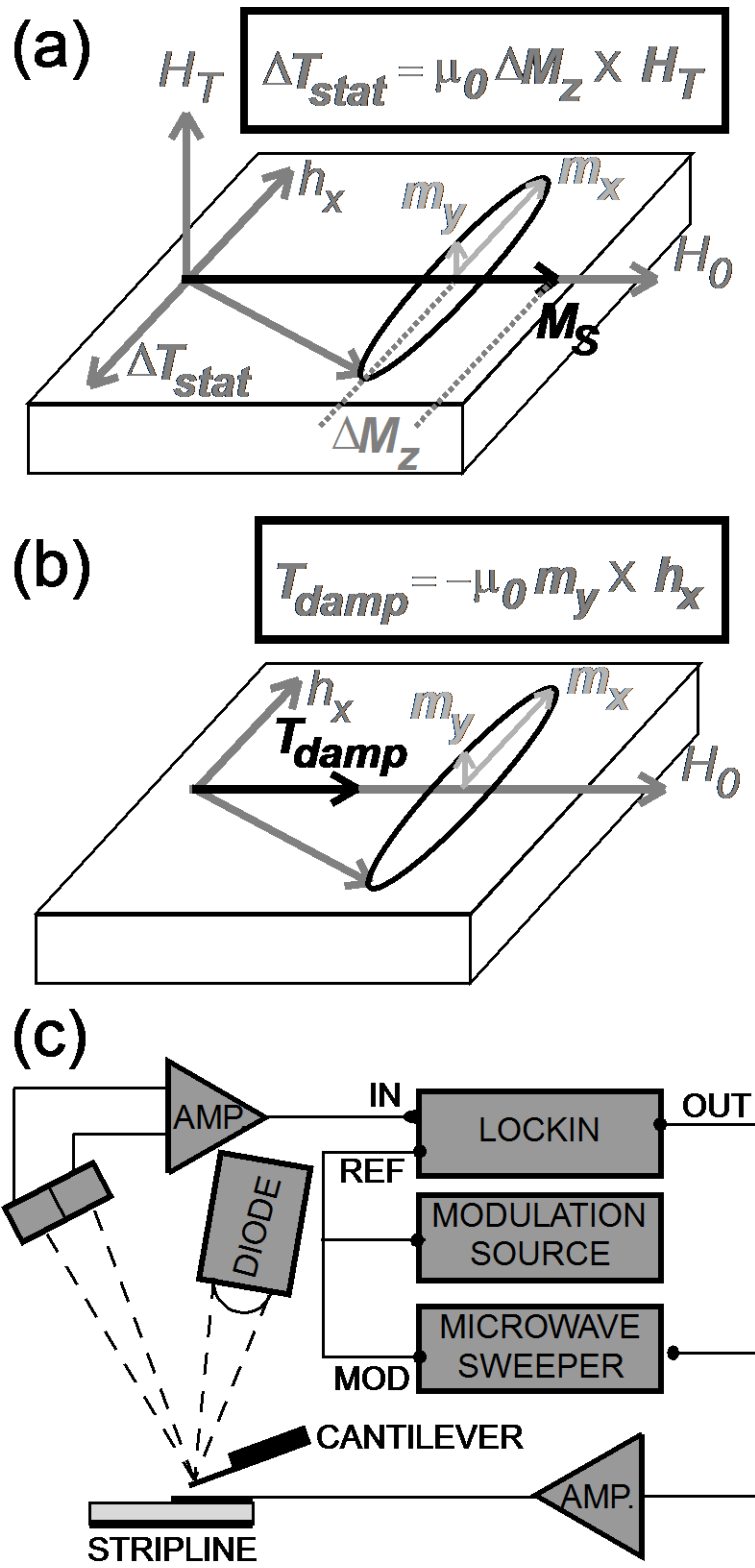


Figure 13.2

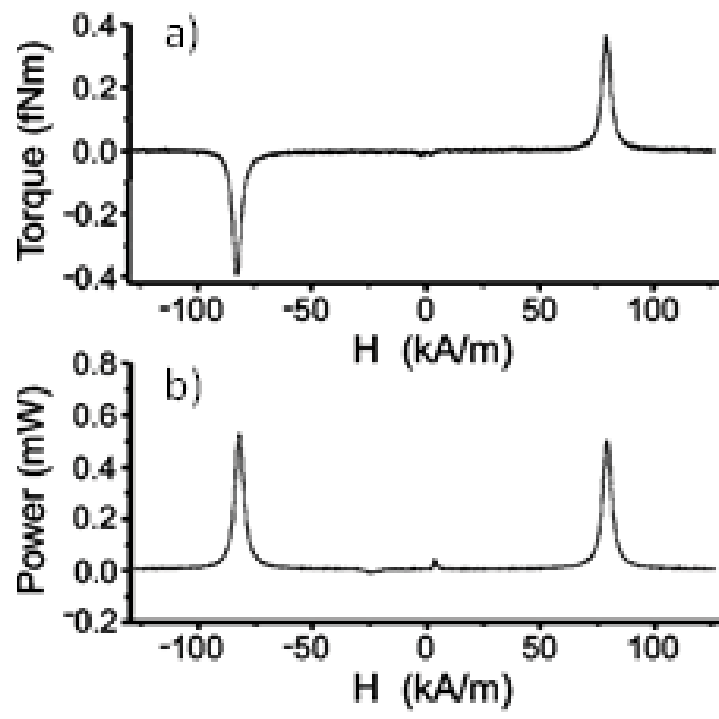


Figure 13.3

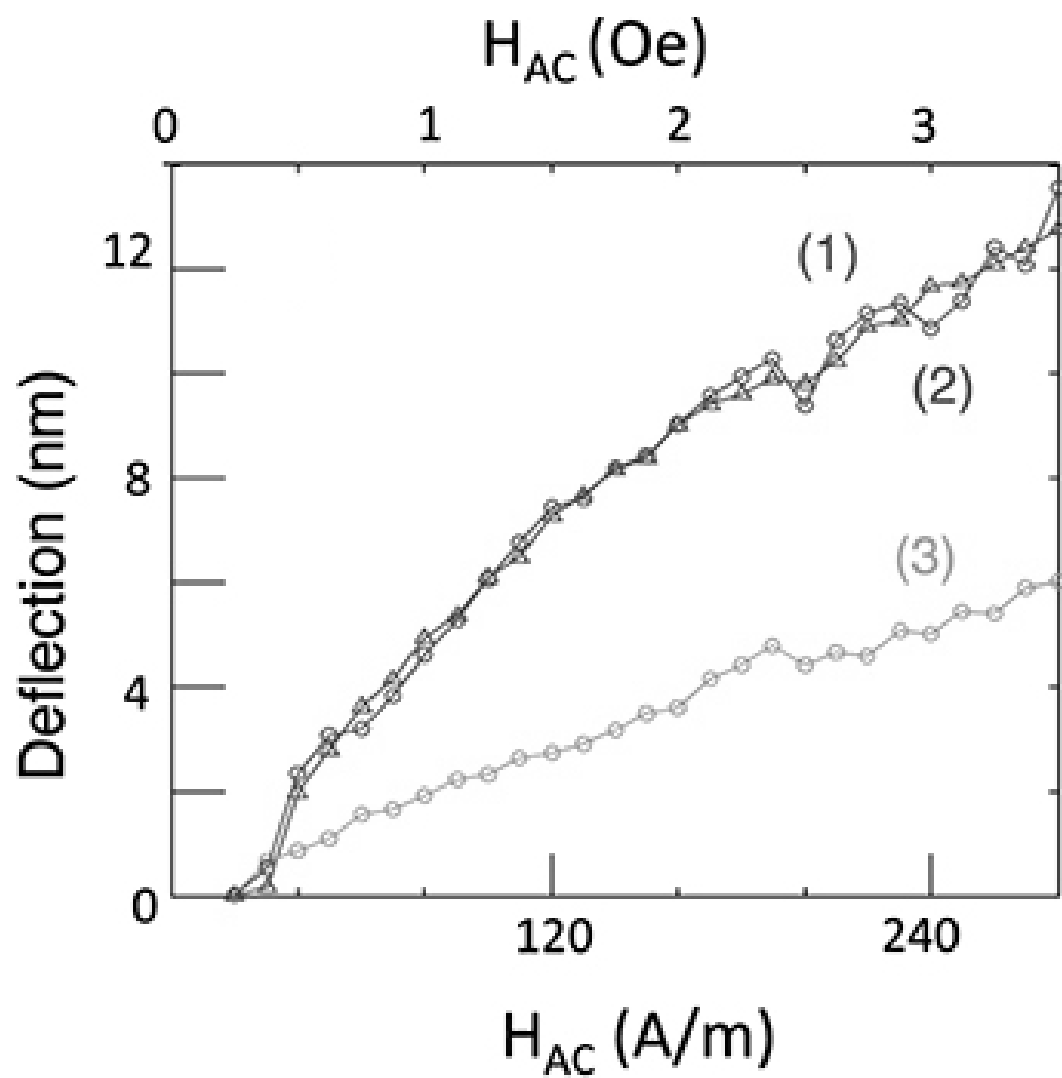


Figure 13.4

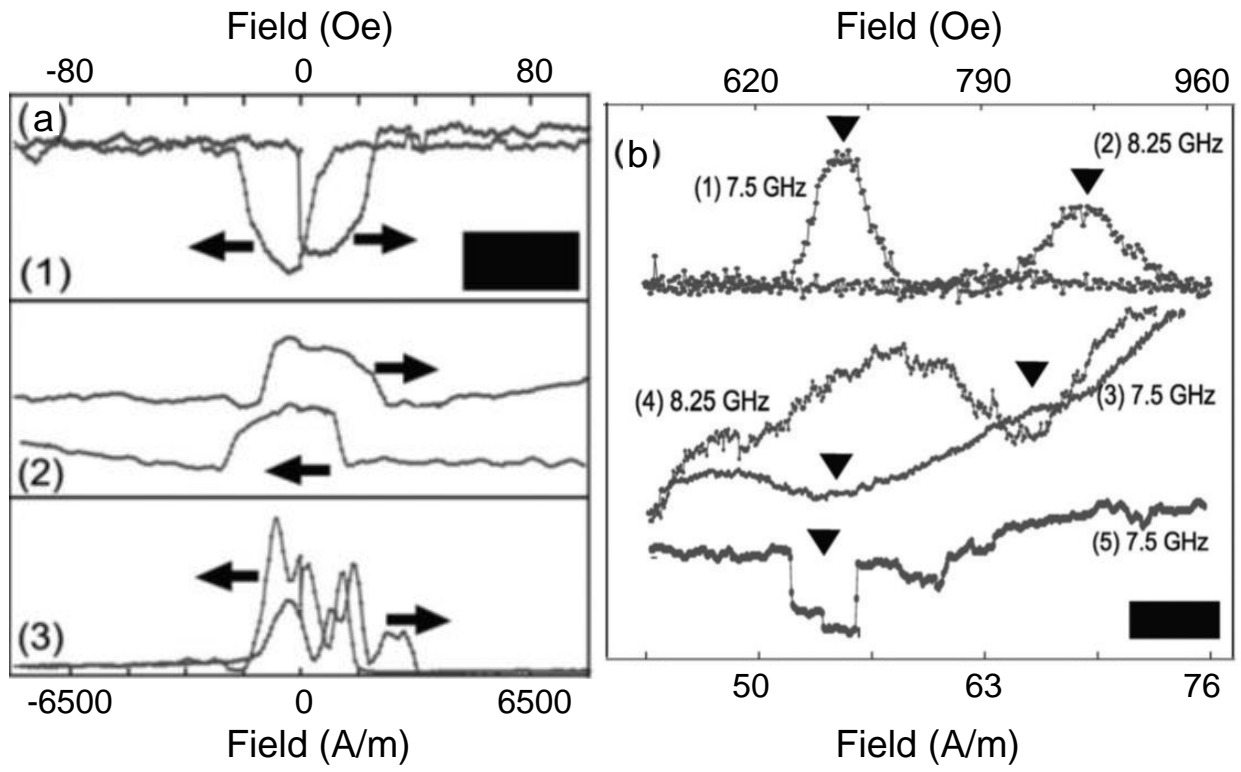


Figure 13.5

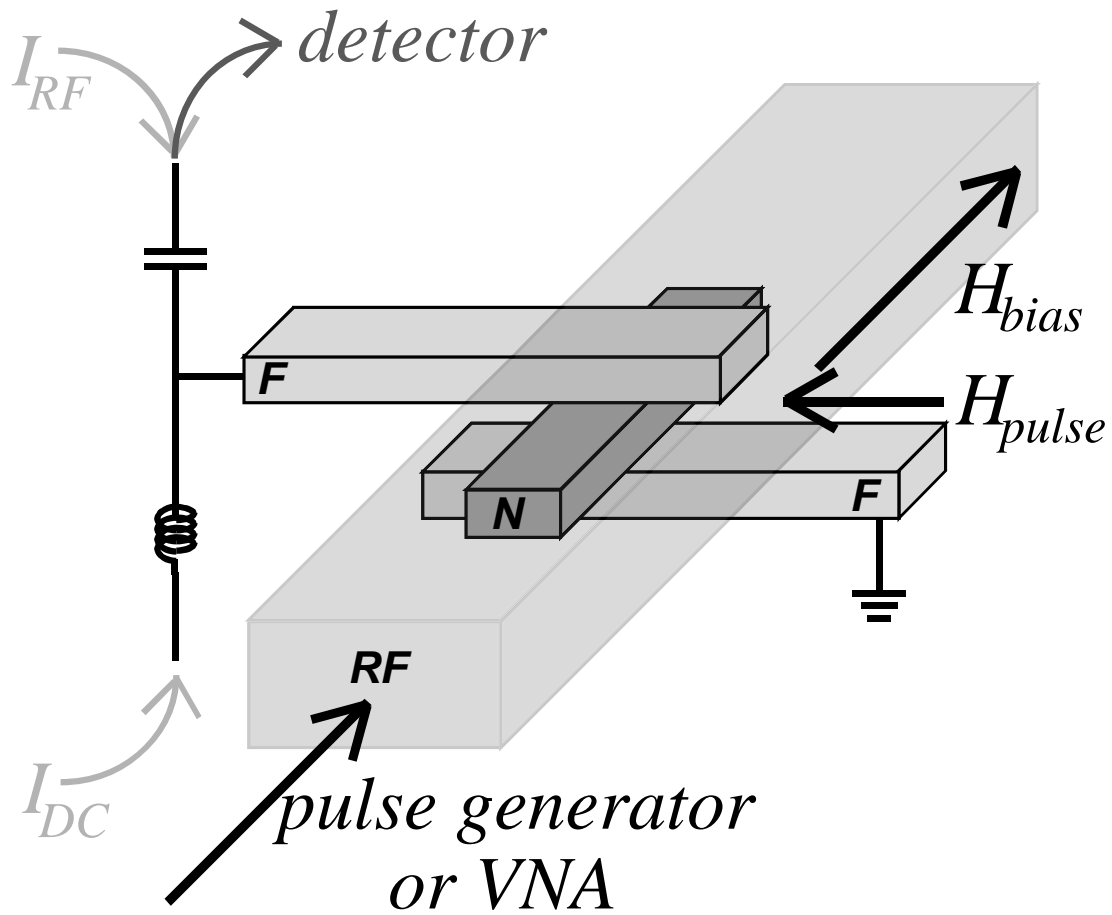


Figure 13.6

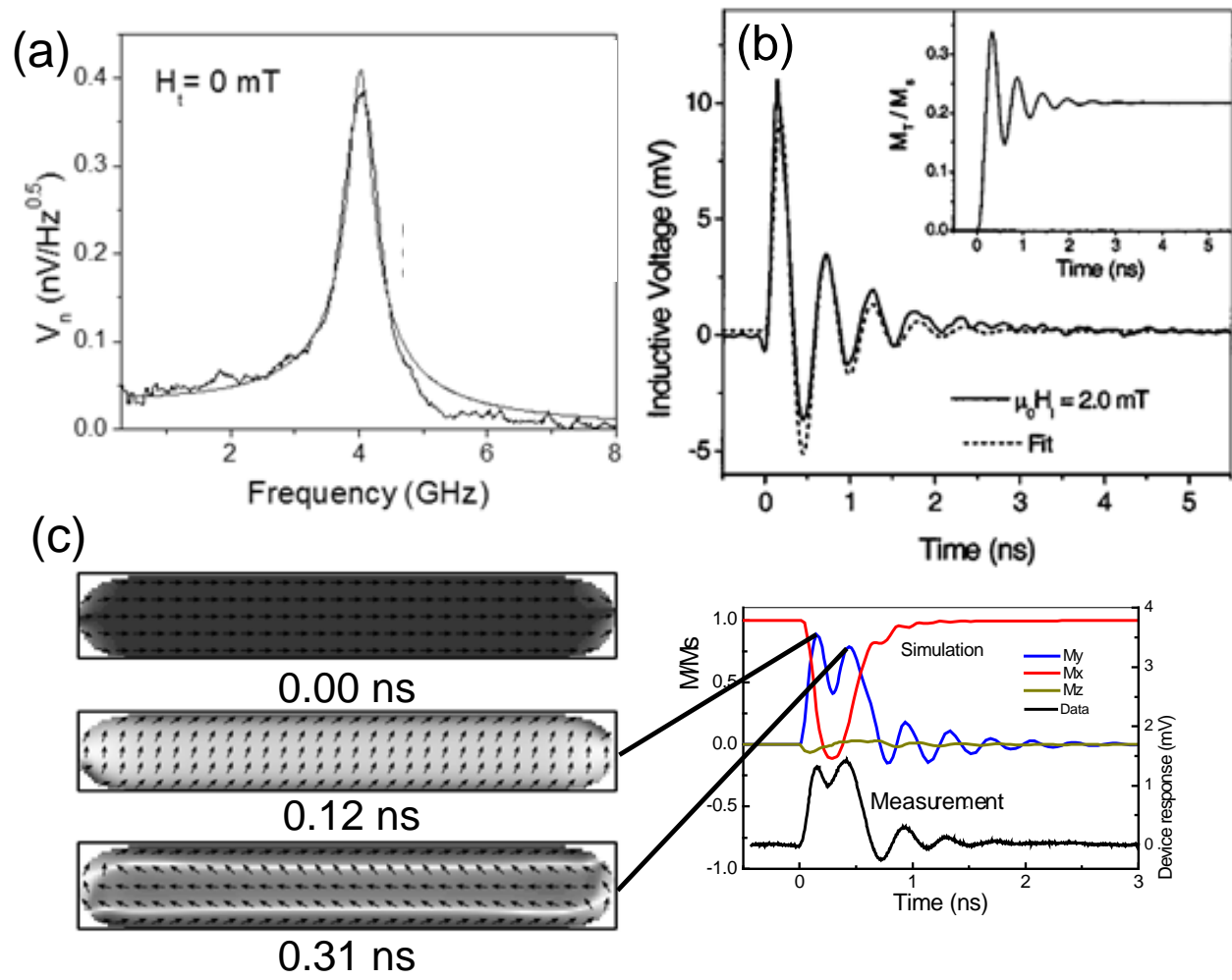


Figure 137

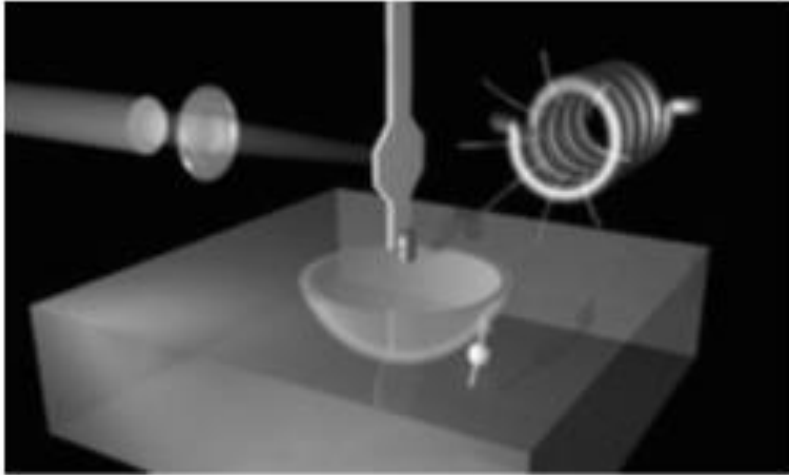


Figure 13.8

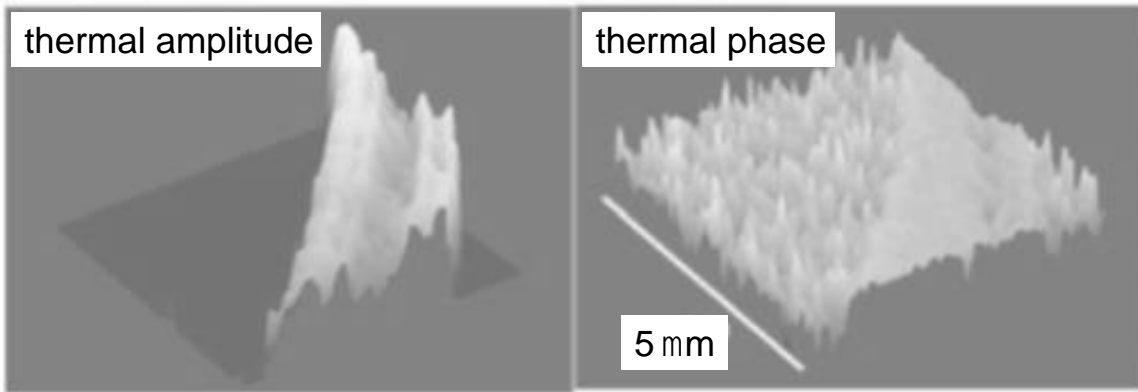


Figure 13.9

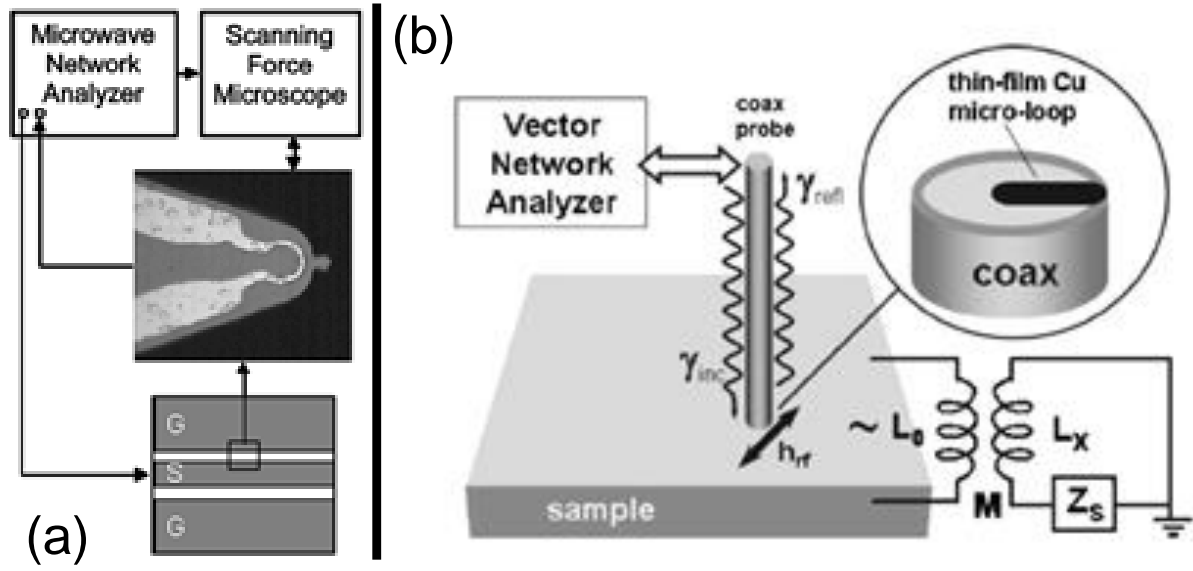


Figure 13.10

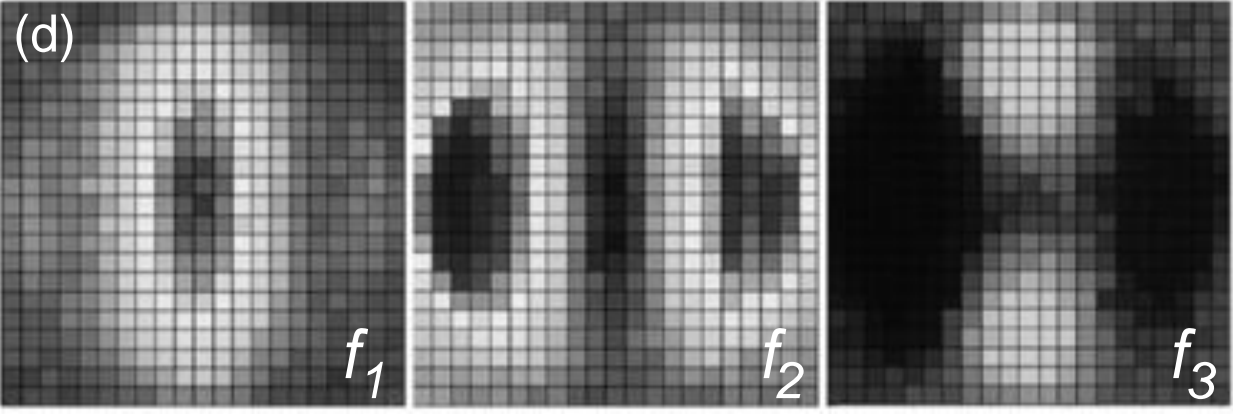
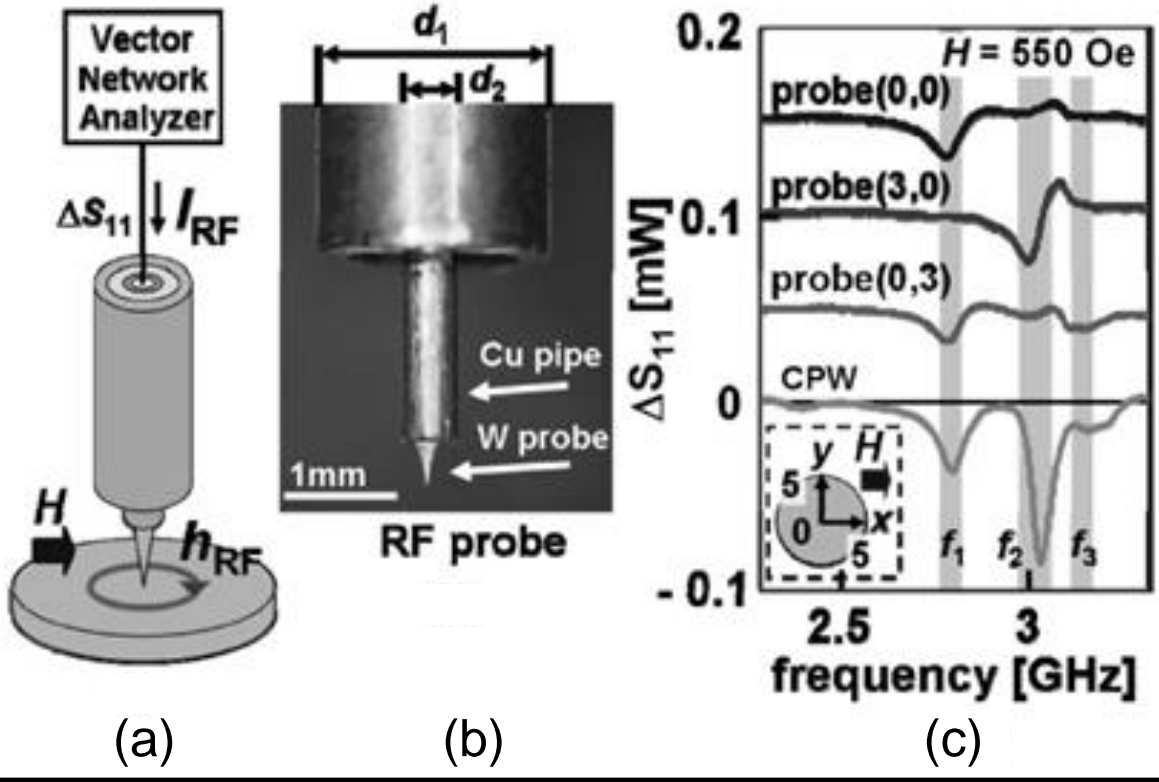


Figure 13.11